

# Mechanical behaviour of additively manufactured metals

Received: 1 December 2024

Accepted: 1 December 2025

Published online: 16 January 2026

 Check for updates

Ting Zhu<sup>1</sup>✉ & Wen Chen<sup>2,3</sup>✉

Additive manufacturing is reshaping the production of engineering components in diverse industries, such as the automotive, aerospace, defence and biomedical sectors, by offering outstanding design and fabrication flexibility. The non-equilibrium processing conditions inherent to additive manufacturing yield materials with unique microstructures and tailored mechanical properties that are often unattainable through conventional routes. This Review highlights recent advances in additively manufactured metals that show distinctive mechanical behaviours, including strength–ductility synergy, microstresses and gradient plasticity, fracture and fatigue resistance, and high-temperature creep performance. We examine the deformation mechanisms and micromechanical effects arising from the heterogeneous microstructures produced by additive manufacturing to guide the design of high-performance structural materials. Furthermore, we discuss critical research needs and emerging opportunities in processing control, alloy design, advanced characterization, computational modelling and machine learning aimed at achieving exceptional mechanical properties in additively manufactured metals.

Additive manufacturing, also known as 3D printing, is revolutionizing global manufacturing industries<sup>1–3</sup>. Additive manufacturing integrates material synthesis and component shaping in a single print, and provides a powerful route for the direct production of end-use parts. By enabling design and fabrication freedoms that were previously unattainable<sup>4</sup>, additive manufacturing has accelerated innovation across various sectors. Exploration of the process–structure–property relationships in additively manufactured (AM) metals presents the materials community with both profound challenges and transformative opportunities<sup>5,6</sup>.

AM metals are typically processed using methods such as laser powder bed fusion (L-PBF) or laser-directed energy deposition (L-DED), which involve intense localized melting and solidification. These processes generate steep temperature gradients ( $10^4$ – $10^7$  K m<sup>-1</sup>) and rapid cooling rates ( $10^3$ – $10^7$  K s<sup>-1</sup>), resulting in non-equilibrium microstructures that substantially influence the material behaviour<sup>1,7</sup>. For example, additive manufacturing enables the creation of hierarchically heterogeneous microstructures, such as submicrometre-scale

coincident chemical and dislocation cells in austenitic stainless steels<sup>8</sup> and dual-phase nanolamellae in eutectic high-entropy alloys (HEAs)<sup>9</sup>. These AM metals show remarkable mechanical properties, including excellent strength–ductility combinations<sup>8–11</sup>, enhanced fracture and fatigue properties<sup>12–14</sup> and ultrahigh creep resistance<sup>15,16</sup>, often outperforming their conventionally manufactured (CM) counterparts.

The microstructural heterogeneity that is inherent to AM metals frequently results in anisotropic and variable mechanical properties<sup>17,18</sup>. Moreover, defects introduced during processing, such as lack-of-fusion pores, keyholes and cracks, can substantially degrade mechanical performance and increase property scatter, in particular the variability and inconsistency observed in measured fracture toughness, fatigue resistance and creep life. Addressing these issues is crucial for the reliable deployment of AM metals in applications that demand high material integrity. Drawing from representative examples of AM metals, this Review examines their mechanical behaviour, focusing on the deformation mechanisms and micromechanical effects that are associated with process-driven microstructures in additive manufacturing.

<sup>1</sup>George W. Woodruff School of Mechanical Engineering, Georgia Institute of Technology, Atlanta, GA, USA. <sup>2</sup>Department of Aerospace and Mechanical Engineering, University of Southern California, Los Angeles, CA, USA. <sup>3</sup>Mork Family Department of Chemical Engineering and Materials Science, University of Southern California, Los Angeles, CA, USA. ✉e-mail: [ting.zhu@me.gatech.edu](mailto:ting.zhu@me.gatech.edu); [wchen001@usc.edu](mailto:wchen001@usc.edu)

## Strength and ductility

Strength and ductility are two key mechanical properties for structural materials, but they are usually in conflict, a phenomenon known as the strength–ductility trade-off. The challenge of simultaneously achieving high tensile strength and ductility can be understood through Considère's criterion for plastic instability<sup>19</sup>. As the tensile flow stress increases with strain, the strain-hardening rate begins to lag behind the geometric softening rate. This effect leads to plastic flow instability, for example, necking, resulting in limited ductility. To improve the balance between strength and ductility, the microstructure needs to be designed with tailored heterogeneities, such as multimodal or gradient grains, twins and other subgrain structures, through thermo-mechanical processing<sup>20,21</sup>. Traditional processing methods—including surface mechanical treatment<sup>22</sup> or rolling with large strains<sup>21</sup>—usually involve severe plastic deformation and are difficult to apply to complex geometries in practical applications.

During additive manufacturing, the line-by-line, layer-by-layer building scheme, along with non-equilibrium solidification conditions, results in unique microstructures compared with conventional processing. Leveraging alloy design with these processing characteristics of additive manufacturing offers a powerful strategy for developing strong and ductile AM materials. A prominent feature of many AM metals is the hierarchically heterogeneous microstructure, which consists of solidification cells with complex structural and chemical heterogeneities that span the microscale to the nanoscale. For example, L-PBF-produced 316L stainless steel has a typical hierarchical microstructure that comprises melt pools, columnar grains, solidification cells, dislocation networks, precipitates and elemental segregation<sup>8</sup> (Fig. 1a–e). These features vary in size from submillimeters to nanometres. Specifically, columnar grains, with lengths of up to ~0.2 mm, grow along the build direction. Subgrain solidification cells, measuring from submicrometres to several micrometres, form due to constitutional supercooling during dendritic solidification<sup>23,24</sup>. This non-equilibrium process leads to elemental partitioning at the liquid–solid interface, creating chemical cells with Mo and Cr segregated at cell walls. In addition, these cell walls contain nano-sized oxides and silicates formed during L-PBF (Fig. 1e), and they collectively trap printing-induced dislocations and act as templates for the formation of dislocation cells (Fig. 1d).

The hierarchical microstructure of AM 316L stainless steel results in high yield strengths of 450–700 MPa and large tensile uniform elongations of 30–60% (Fig. 1f), a much better strength–ductility balance than those of the CM 316L stainless steel counterparts (Fig. 1g). The hierarchical microstructure provides multiple strengthening effects in AM 316L stainless steel. The submicrometre solidification cells refine the microstructure and impart strong strengthening. As-printed dislocation cell walls contain a high density of dislocations, contributing further to the strengthening. In addition, solute segregation and nanoprecipitates at the cell walls stabilize the dislocation cell structures, promoting dislocation pinning and twinning during plastic deformation. These factors collectively enable high rates of strain hardening during the early stages of plastic deformation. Moreover, interactions between deformation twins and solidification cells create a three-dimensional (3D) network of obstacles that impede dislocation motion, sustaining the high strain-hardening rate as the flow stress increases and resulting in enhanced ductility<sup>8</sup>.

Hierarchically heterogeneous microstructures are also formed in other AM metals, including precipitation-hardened steels<sup>25,26</sup>, Al alloys<sup>27</sup>, Ti alloys<sup>10,28,29</sup>, Ni-based superalloys<sup>30</sup> and HEAs<sup>31</sup>, enhancing their strength–ductility balance. Another notable example is a series of L-DED-produced Ti–Cu alloys with ultrafine eutectoid nanolamellae in equiaxed grains<sup>28</sup> (Fig. 1h). The Cu alloying element undergoes strong partitioning during solidification, inducing a large constitutional supercooling zone ahead of the solid–liquid interface. This process promotes the columnar-to-equiaxed transition of the grain

structure, resulting in equiaxed prior- $\beta$  grains with an average size of ~10  $\mu\text{m}$ —much smaller than the columnar grains that are typically observed in other AM Ti alloys. As a consequence of the rapid cooling and thermal cycling that are inherent to layer-by-layer printing, these prior- $\beta$  grains decompose into  $\alpha$ -Ti and  $\text{Ti}_2\text{Cu}$  through a solid-state eutectoid reaction, resulting in dual-phase eutectoid nanolamellae. The average interlamellar spacing in the as-printed Ti–8.5Cu alloy (Ti with 8.5 wt% Cu) is ~50 nm, substantially finer than the 0.15–1  $\mu\text{m}$  spacing observed in CM counterparts<sup>28</sup>. The AM Ti–Cu alloys with this ultrafine eutectoid lamellar structure have an excellent combination of yield strength and ductility compared with both conventional Ti–Cu and the more expensive Ti–6Al–4V (that is, 90 wt% Ti, 6 wt% Al, 4 wt% V) alloys in CM and AM forms<sup>28</sup> (Fig. 1i).

Controlling the printing process in AM alloys enables the tailoring of grain structures, allowing transitions from columnar to equiaxed grains and producing finer grains that improve the strength and ductility. Printing parameters such as the laser power, scan speed, scan pattern and substrate temperature affect the temperature gradient ( $G$ ) and growth rate ( $R$ ) during solidification. These factors affect the degree of constitutional supercooling, which determines the resulting microstructure. Generally, a higher laser power, a slower scan speed or a preheated substrate lowers the  $G$  value<sup>6,32</sup>. Non-linear or alternating scan patterns (for example, rotating the scan direction between neighbouring layers) help to distribute heat more evenly, reducing  $G$  and thermal stresses<sup>5</sup>. By contrast,  $R$  is mainly controlled by the scan speed and increases with it. The  $G/R$  ratio governs the microstructural morphology, whereas the  $G \times R$  product (that is, the cooling rate) influences the feature size<sup>1</sup>. Lower  $G/R$  values and higher cooling rates promote fine equiaxed grains with reduced texture, improving the strength–ductility combinations in AM alloys<sup>33–35</sup>. Introducing nucleation inoculants, either ex-situ-doped or in-situ-formed nanoparticles, is another effective strategy for achieving fine equiaxed grains<sup>36–39</sup>. For example, AM 7075 and 6061 Al alloys are prone to solidification cracking due to their persistent columnar dendritic structures and wide freezing ranges<sup>37</sup>. Adding lattice-matched Zr nanoparticles, which provide a high density of low-energy-barrier heterogeneous nucleation sites ahead of the solidification front, promotes the formation of fine equiaxed grains, reducing thermal strains and preventing cracks. This approach produces crack-free microstructures with ~5  $\mu\text{m}$  grains, much finer than the untreated columnar grains<sup>37</sup>. The strength and ductility of these inoculated AM Al alloys are substantially enhanced compared with their unmodified counterparts and are comparable to those of wrought alloys. This strategy is broadly applicable to other materials, such as non-weldable Ni superalloys<sup>40</sup>, Ti alloys<sup>11</sup> and HEAs<sup>41</sup>, advancing AM metals with superior mechanical properties.

## Microstress and gradient plasticity

At the microscale, materials develop self-equilibrating internal stresses—often called microstresses—that arise from microstructural heterogeneity. A key micromechanical effect in AM metals is the generation of intergranular and intragranular microstresses<sup>42</sup>. Substantial strengthening can be achieved by enhancing these microstresses in hierarchically heterogeneous microstructures<sup>43–46</sup>. When a polycrystal is loaded, macrostress develops at the sample level, whereas intergranular microstresses arise between grains (Fig. 2a). These intergranular microstresses are internal stresses that fluctuate across grains to maintain self-equilibrium. As the load increases, stiffer grains bear more load, resulting in higher positive intergranular microstresses. Conversely, softer grains experience larger negative intergranular microstresses. Within each grain, intragranular microstresses develop due to local lattice distortions caused by dislocation substructures, chemical modulation, precipitate particles or co-existing phases. These intragranular microstresses also fluctuate within individual grains and increase with the applied load (Fig. 2a). The evolution of intergranular stresses is strongly influenced by the co-evolution of intragranular stresses<sup>42</sup>.

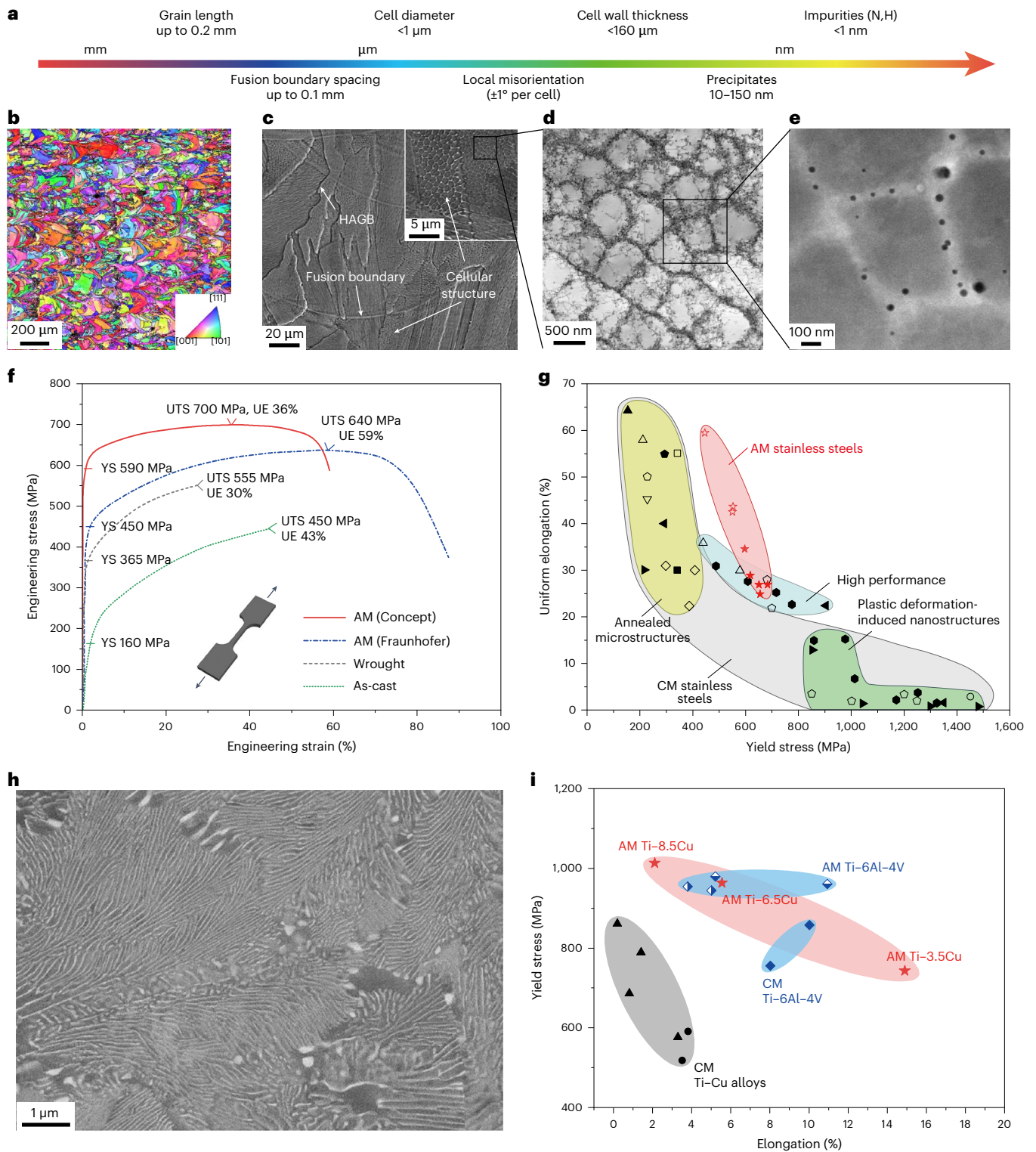


**Fig. 1 | Hierarchical microstructure and tensile properties of AM 316L stainless steels and Ti–Cu alloys.** **a**, Schematic of various microstructural length scales in L-PBF-produced 316L stainless steels. **b**, Cross-sectional electron backscatter diffraction inverse pole figure map of the L-PBF-produced 316L stainless steel sample. **c**, Cross-sectional scanning electron microscopy image showing melt pool or fusion boundaries, high-angle grain boundaries (HAGBs) and solidification cellular structures. The inset shows the cellular structure at a higher magnification. **d**, Bright-field transmission electron microscopy (TEM) image of solidification cells. **e**, High-angle annular dark-field scanning TEM image of the solidification cells shown in **d**. Oxide and silicate nanoparticles were formed and segregated at the cell walls during L-PBF processing. **f**, Representative tensile stress–strain curves for two L-PBF-produced 316L stainless steels

(fabricated using the Concept and Fraunhofer printing machines, respectively), compared with those of as-cast and wrought materials. The yield strength (YS), uniform elongation (UE) and ultimate tensile strength (UTS) are marked on the curves. The inset shows a schematic of the tensile specimen. **g**, Summary of uniform elongation versus yield stress for AM 316L stainless steels compared with traditional counterparts. **h**, Backscattered electron image of the L-DED-produced Ti–8.5Cu alloy, showing fine nanolamellar eutectoid colonies surrounded by hyper-eutectoid  $\text{Ti}_2\text{Cu}$  particles. **i**, Yield stress versus elongation for AM Ti–Cu alloys compared with CM Ti–Cu counterparts and AM and CM Ti–6Al–4V alloys. The specific alloys corresponding to the data points are from ref. 28. Panels adapted with permission from: **a–g**, ref. 8, Springer Nature Limited; **h, i**, ref. 28, Springer Nature Limited.

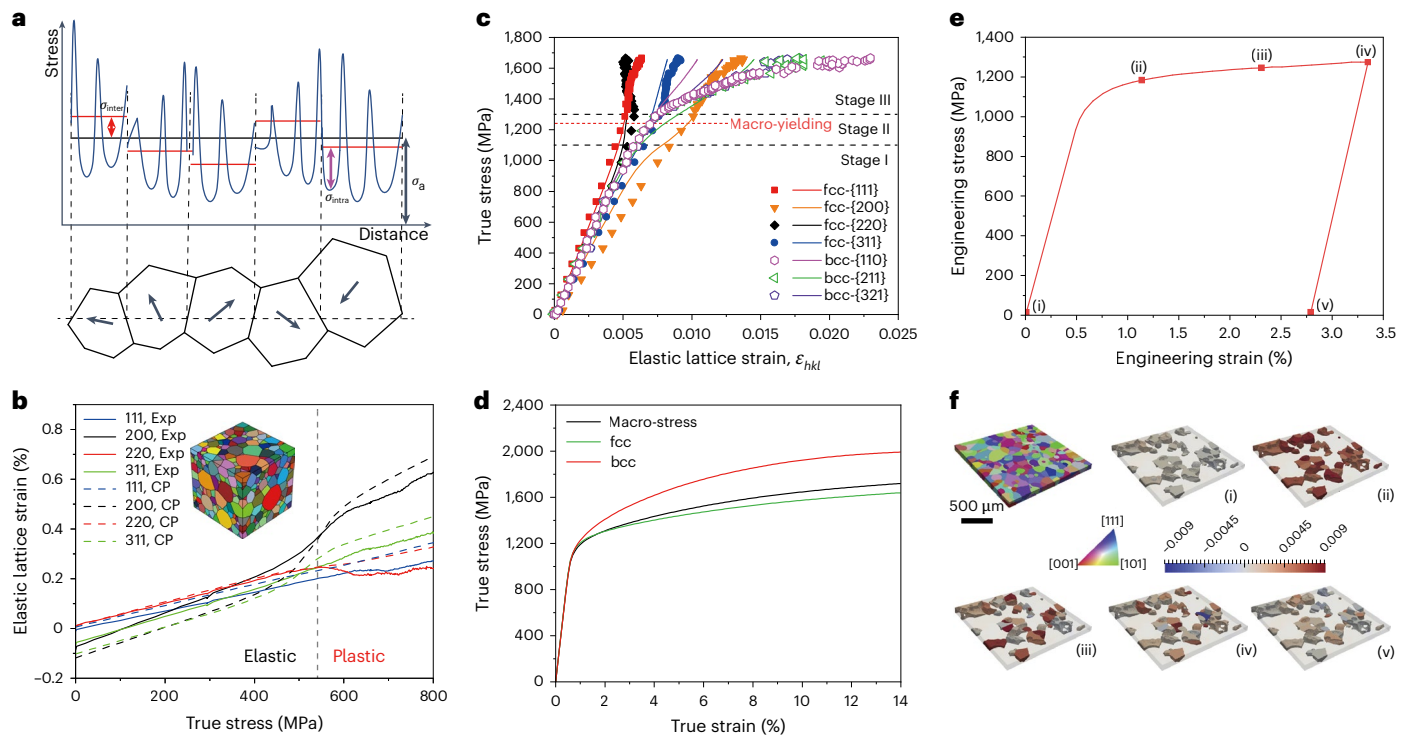


**Fig. 2 | Characterization and modelling of microstresses in AM metals.**

**a**, Schematic of the intergranular ( $\sigma_{inter}$ ) and intragranular ( $\sigma_{intra}$ ) stresses occurring at different microstructural length scales when a polycrystal is subjected to an applied stress ( $\sigma_a$ ). The black arrows denote the different crystallographic orientations of the grains. **b**, Comparison of the lattice strains along the loading direction against the macroscopic true stress for the  $\{111\}$ ,  $\{200\}$ ,  $\{220\}$  and  $\{311\}$  grain families in an L-PBF-produced 316L stainless steel from in situ synchrotron X-ray diffraction experiments (Exp) and CPFE simulations (CP)<sup>47</sup>. The inset shows a schematic of the polycrystal sample. **c**, Evolution of lattice strain against macroscopic true stress for representative fcc and bcc crystallographic plane families in an L-PBF-produced AlCoCrFeNi<sub>2.1</sub> eutectic HEA along the loading direction from in situ neutron diffraction

experiments (data points) and CPFE simulations (solid lines)<sup>9</sup>. The red dashed line indicates the macroscopic yield stress of the sample. **d**, Dual-phase CPFE simulation results of the macroscopic stress–strain response (black) with the corresponding stress partitioning in the fcc (green) and bcc (red) phases of the L-PBF-produced AlCoCrFeNi<sub>2.1</sub> eutectic HEA<sup>9</sup>. **e**, Tensile stress–strain curve of an AM IN718 sample, where the marked states (i)–(v) correspond to the different stress states at which in situ HEDM scans were conducted to assess lattice strains in the sample<sup>50</sup>. **f**, Three-dimensional HEDM images of the AM IN718 sample (main image top left), in which 70 grains were tracked at the different stress states from (i) to (v) as shown in **e**. The elastic strain component along the loading direction is illustrated by the colour scale. Panels adapted with permission from: **b**, ref. 47, Springer Nature Limited; **c,d**, ref. 9, Springer Nature Limited; **e,f**, ref. 50, Elsevier.

Advanced in situ experimental techniques, including high-energy synchrotron X-ray or neutron diffraction, have been used to quantitatively characterize intergranular microstresses. These techniques track changes in lattice spacing for each family of grains with a common crystallographic orientation under load, enabling the determination of lattice strains. Intergranular stresses in these grain families are calculated by multiplying lattice strains by the corresponding diffraction elastic constant<sup>42</sup>. For example, synchrotron X-ray measurements of lattice strains in representative grain families have been conducted before and during the tensile loading of an L-PBF 316L stainless steel sample<sup>47</sup> (Fig. 2b). The non-zero lattice strains observed before loading indicate residual intergranular microstresses in the as-printed state. These residual microstresses arise from geometric incompatibilities among neighbouring grains from rapid solidification, reflecting how extreme printing conditions contribute to microstress generation. During tensile loading, the lattice strains of these grain families initially show an anisotropic linear response, followed by non-linear downturn and upturn behaviours from the plastically softer  $\{220\}$  to the harder  $\{200\}$  grain families. These results indicate load shedding and redistribution among different grain families during their progressive yielding and strain hardening. As shown in Fig. 2b, the simulated lattice strains from a crystal plasticity finite element (CPFE) model agree with the experimental data<sup>47</sup>. This model accounts for both intergranular and intragranular microstresses, enabling the quantitative evaluation of the residual intergranular

microstresses and the varying elastic–plastic responses of the grain families during loading.

Understanding the microstress effects often requires the quantitative tracking of load partitioning among different phase components in heterogeneous microstructures. Neutron diffraction measurements of lattice strains have been performed on an AM AlCoCrFeNi<sub>2.1</sub> eutectic HEA (Fig. 2c), which features a hierarchical microstructure that consists of alternating face-centred cubic (fcc) and body-centred cubic (bcc) nanolamellae embedded within micrometre-sized eutectic colonies<sup>9</sup>. The lattice strains in representative fcc and bcc grain families show varying elastic–plastic responses due to load shedding and redistribution as the applied load is increased. The simulated lattice strains from a dual-phase CPFE model (Fig. 2c) agree well with the experimental data. This model enables the tracking of the average stress–strain responses of individual fcc and bcc phases in the nanolamellar eutectic colonies. Both the bcc and fcc nanolamellae have high strengths and notably high strain-hardening rates, achieving up to 14% uniform tensile strain (Fig. 2d). The bcc nanolamellae contribute more substantially to the overall strain-hardening response than the fcc nanolamellae, thereby promoting high tensile ductility. Typically, bcc nanostructures alone exhibit high strength but low ductility. However, in this AM eutectic HEA, high strain hardening in the bcc nanolamellae is enabled by the constraining effects of the ductile fcc nanolamellae. This combination of high strength and ductility in bcc nanostructures is rarely achieved in traditional materials<sup>48</sup>.

To resolve the spatial distribution of intergranular microstresses in AM metals, in situ high-energy X-ray diffraction microscopy (HEDM) has been used to carry out grain-by-grain measurements of lattice strain responses<sup>49</sup>. For the Ni-based superalloy of Inconel 718 (IN718) produced via L-PBF, Fig. 2e shows the tensile stress–strain curve with marked stress states (i)–(v). Far-field HEDM was used to assess grain-by-grain lattice strains at these stress states in the tensile specimen<sup>50</sup>. A reconstructed orientation map of 451 grains is presented in the top left of Fig. 2f, colour-coded according to the inverse pole figure, from a volume of 1.5 mm × 1.5 mm × 90 μm. Lattice strains were tracked for 70 grains during tensile loading and unloading (Fig. 2f(i)–(v)). This HEDM characterization directly reveals the average lattice strains of individual grains in a bulk sample. It can also be combined with other spatial mapping techniques, such as digital image correlation and electron backscatter diffraction<sup>51</sup>, to explore how neighbouring grains influence microscale deformation and the associated microstresses in individual grains.

An approach to characterize the overall strengthening effects of intragranular microstresses is to measure the sample-level back stress. For example, in AM 316L stainless steel, dislocation cells form within grains (Fig. 1b–d). The cell walls are hard regions with high dislocation densities, whereas the cell interiors are softer. This combination of hard and soft domains generates substantial intragranular microstresses, resulting in substantial enhancements of the sample-level flow stress. To characterize these microstresses, the total flow stress can be divided into effective stress and back stress<sup>47</sup>. The effective stress represents non-directional, short-range resistance to dislocation glide in the cell interiors, caused by lattice friction and local pinning from forest dislocations. By contrast, the back stress represents directional, long-range resistance within the cell interiors. This resistance results from gradient plasticity involving local plastic strain gradients and geometrically necessary dislocations (GNDs), which form to accommodate deformation incompatibilities between the hard and soft regions within grains. Grain boundaries also act as hard regions and contribute to the back stress<sup>52</sup>. For AM 316L stainless steel (Fig. 1a–g), the measured back stress at the sample level is ~300 MPa, accounting for ~50% of its flow stress<sup>8</sup>. This substantial back stress reflects strong intragranular microstresses and contributes to the excellent combination of high strength and ductility in this AM material. A similar effect is observed in the AM AlCoCrFeNi<sub>2.1</sub> eutectic HEA, where the measured back stress is ~1,000 MPa, accounting for ~65% of its tensile flow stress<sup>9</sup>. The high back stress arises from the alternating fcc and bcc nanolamellar structure. It should be noted that the sample-level back stress is an average of spatially varying back stresses in heterogeneous microstructures, and these back stresses can be tailored to optimize their impact on mechanical performance<sup>43–46</sup>.

The back-stress strengthening effects in AM stainless steel and eutectic HEA largely stem from their heterogeneous microstructures, which generate strong gradient plasticity and associated GNDs during loading. Additive manufacturing offers a unique capability to promote these effects by creating site-specific heterogeneous microstructures via adjustments in processing parameters or feedstock materials<sup>26,53</sup>. For example, a study improved the mechanical properties of AM 316L stainless steel by programming recrystallization via heat treatment<sup>54</sup>. Two L-PBF processing strategies, denoted as ‘H’ (high thermal stability due to single-layer scanning with a large hatch spacing) and ‘L’ (low thermal stability due to rescanning with a small hatch spacing), were used to create layered microstructures with non-recrystallized and recrystallized regions, respectively. The heat-treated samples in Fig. 3a have similar volume fractions of non-recrystallized and recrystallized regions with various layer thicknesses. The fully recrystallized microstructure has a yield strength of 322 MPa and a uniform elongation of 46%, whereas the non-recrystallized structure has a yield strength of 440 MPa and a uniform elongation of 32% (Fig. 3b). The tensile behaviour of the layered microstructures (Fig. 3a) is also shown (Fig. 3b). The

yield strength of both coarse and fine layered architectures follows the rule of mixtures. However, the fine architecture achieves an ultimate tensile strength of 708 MPa, about 20 MPa higher than the coarse architecture. This strength increment is attributed to the effects of gradient plasticity and the associated GNDs that accommodate strain incompatibilities between soft and hard layers (Fig. 3c), resulting in enhanced back-stress strengthening and strain hardening (Fig. 3d). Notably, studies on gradient-structured metals have established a systematic framework for characterizing and understanding gradient plasticity in gradient microstructures<sup>43–46</sup>, laying a foundation for further investigation into the strengthening and strain-hardening effects of site-specific heterogeneous microstructures in AM metals.

## Fracture and fatigue

Fracture toughness and fatigue resistance reflect how well a material can resist cracking, and these properties in AM metals are crucial for structural integrity<sup>55</sup>. Unlike strength and ductility, which can be readily measured via tensile tests, assessing fracture toughness and fatigue resistance requires more complex sample preparation and testing protocols. Although fracture toughness and tensile ductility are sometimes linked, studies have often shown a weak correlation between these two properties, especially in AM metals<sup>56</sup>. For example, a wide range of fracture toughness values (16–32 MPa m<sup>1/2</sup>) has been reported for L-PBF-produced A357 Al alloys depending on the test orientation, despite consistent ductility values (6.9–7.6%) across all orientations<sup>57</sup>. This weak correlation, along with remarkable variations in the fracture toughness of AM metals, arises from the sensitivity of fracture toughness to processing defects and heterogeneous microstructures.

Processing defects such as lack-of-fusion pores, keyholes and solidification cracks are common in AM metals<sup>58</sup>. These defects can result from flaws in the powder feedstock, improper fusion energy or process instability during laser–powder interaction, often reducing the fracture toughness and causing variability. To mitigate this issue, process optimization and post-processing heat treatment are frequently used to reduce defects and residual stresses. For instance, low fracture toughness values of 16–28 MPa m<sup>1/2</sup> were reported for L-PBF-produced Ti–6Al–4V alloys due to printing defects and residual stresses<sup>59</sup>. After process optimization and heat treatment, near-full density (>99.5%) was achieved and the fracture toughness increased to 48–58 MPa m<sup>1/2</sup>, which is comparable to 44–66 MPa m<sup>1/2</sup> for CM counterparts<sup>60</sup>.

The heterogeneous microstructure of AM metals also affects their fracture behaviour. For example, melt pool boundaries cause anisotropy in fracture toughness. In Fig. 4a, L-PBF-produced AlSi10Mg alloys (that is, Al alloys with 10 wt% Si and 0.3 wt% Mg) tested in orientations parallel and perpendicular to the build direction show fracture toughness values of 20–30 MPa m<sup>1/2</sup>, which exceed the ~19 MPa m<sup>1/2</sup> observed in conventionally processed counterparts<sup>27</sup>. The melt pool boundaries are generally oriented perpendicular to the build direction. As a result, cracks propagating along the build direction are frequently deflected by these boundaries (Fig. 4b), resulting in substantial crack path tortuosity and enhanced fracture toughness. By contrast, when a crack propagates perpendicular to the build direction, it tends to align closely with the melt pool boundaries (Fig. 4c), leading to anisotropic and reduced fracture toughness.

Solidification cells are another type of heterogeneous microstructure in AM metals that affects their fracture behaviour. Dislocation networks and elemental segregation at cell walls provide an intrinsic toughening mechanism that delays fracture. A recent study has shown that the cellular structures in an L-PBF-produced CoCrFeNiAl<sub>0.5</sub> HEA consist of CoCrFe-rich fcc cell interiors and NiAl-rich bcc/B2 nanoprecipitates at fcc cell walls<sup>32</sup> (Fig. 4d,e). These nanoprecipitates are connected by ‘nano-bridges’ of high dislocation density at the cell walls. The nanoprecipitates limit dislocation movement, enhancing the strength, while the nano-bridges allow dislocations to pass, improving fracture resistance by reducing the strain concentration at the crack tip.

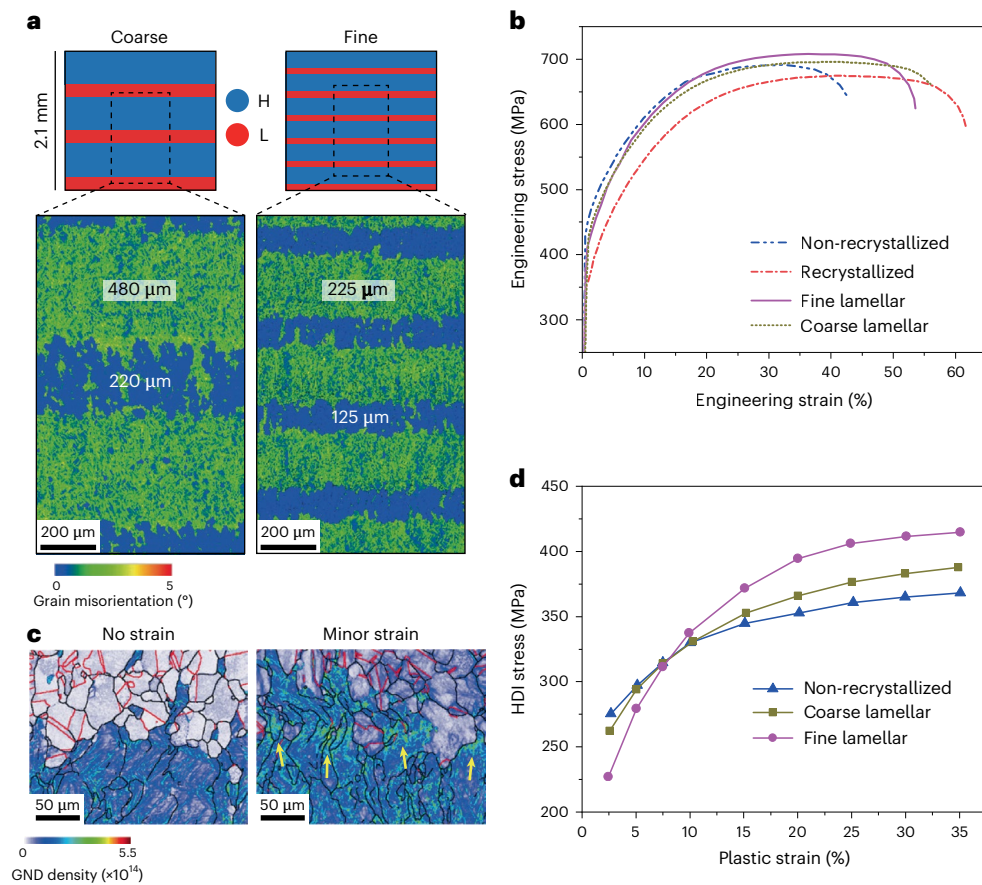


**Fig. 3 | Strain gradient plasticity and back-stress strengthening in AM 316L stainless steels with layered microstructures.** **a**, Print design (top) and corresponding electron backscatter diffraction kernel average misorientation maps (bottom) of coarse and fine layered microstructures. **b**, Tensile stress-strain curves of the non-recrystallized, fully recrystallized and layered microstructures. **c**, GND maps measured via electron backscatter diffraction,

showing pile-ups (marked by yellow arrows) at the interface between the two microstructure constituents upon loading in the sample with a fine layered architecture. **d**, Evolution of back stress or heterodeformation-induced (HDI) stress of the different samples as a function of plastic strain. Panels **a–d** adapted with permission from ref. 54, Springer Nature Limited.

This combination leads to high strength ( $\sim 1$  GPa) and fracture toughness ( $\sim 300$  MPa  $m^{1/2}$ ), outperforming most CM alloys<sup>12</sup>.

The fatigue resistance of AM metals is strongly influenced by their solidification cellular structures. As shown in Fig. 4f–h, the microstructure of nano-TiB<sub>2</sub>-decorated AlSi10Mg (NTD-Al) alloy produced via L-PBF forms dual-phase cells, with Al-rich fcc cell interiors and a Si-rich secondary intermetallic phase at the cell walls<sup>13</sup>. These cellular structures, approximately 500 nm in size, act as volumetric dislocation barriers, confining dislocation movement under cyclic loading (Fig. 4i). This confinement impedes long-range dislocation slip and reorganization, reducing the accumulation of localized fatigue damage<sup>13</sup>.

The excellent fatigue resistance of AM NTD-Al is also attributed to the mitigation of printing defects. Studies have shown that the fatigue performance of AM metals is generally lower than those of CM counterparts due to printing defects that act as stress concentration sites, accelerating fatigue crack initiation and growth<sup>61</sup>. The characteristics of these defects, including shape, size and spatial distribution, strongly affect the fatigue resistance. Lack-of-fusion pores are particularly harmful due to their large size and high aspect ratio. For example, in typical AM AlSi10Mg alloys<sup>13</sup>, these pores are often irregular and can reach hundreds of micrometres in size (Fig. 4j). Such flaws can dominate the fatigue behaviour of AM metals, leading to reduced fatigue resistance with high variability<sup>62</sup>. In AM NTD-Al alloy<sup>13</sup>, the addition of TiB<sub>2</sub> nanoparticles during L-PBF effectively mitigates the formation of large lack-of-fusion defects, resulting in nearly spherical pores that are only tens of micrometres in size (Fig. 4k). Recent in situ high-speed synchrotron X-ray

imaging has revealed that these nanoparticles stabilize melt pools and prevent the coalescence of liquid droplets, reducing large spatters and minimizing lack-of-fusion pores<sup>63</sup>. The reduction in printing defects enhances the dislocation storage capability of the cellular nanostructures previously mentioned. As a result, AMNTD-Al achieves an excellent fatigue strength limit of  $\sim 250$  MPa, which is nearly double that of both CM and AM AlSi10Mg counterparts<sup>13,64–68</sup> (Fig. 4l). This improvement is even more pronounced in defect-free microscale samples of AMNTD-Al, which exhibit an ultrahigh intrinsic fatigue strength limit that exceeds 470 MPa and a fatigue strength ratio of  $\sim 0.9$  (ref. 13; Fig. 4l).

Similarly, a recent study on L-PBF-produced Ti–6Al–4V alloys has demonstrated that an optimized post-printing treatment—involving a multi-step heat-treatment schedule and hot isostatic pressing—successfully removed detrimental lack-of-fusion pores, resulting in a nearly void-free microstructure<sup>14</sup>. This defect-lean AM Ti–6Al–4V exhibits an outstanding fatigue limit of  $\sim 1$  GPa, which is at least 20% higher than other AM Ti alloys and their traditionally forged counterparts<sup>14</sup>. These studies highlight the effect of printing defects on the fatigue performance of AM metals, underscoring the importance of process control to reduce defects.

## Creep and rupture

Creep is the slow deformation of materials over time under constant stress at elevated temperatures. The creep behaviour of AM metals has not been thoroughly investigated due to the lengthy testing required. Most studies focus on Ni-based superalloys, in particular IN718, which

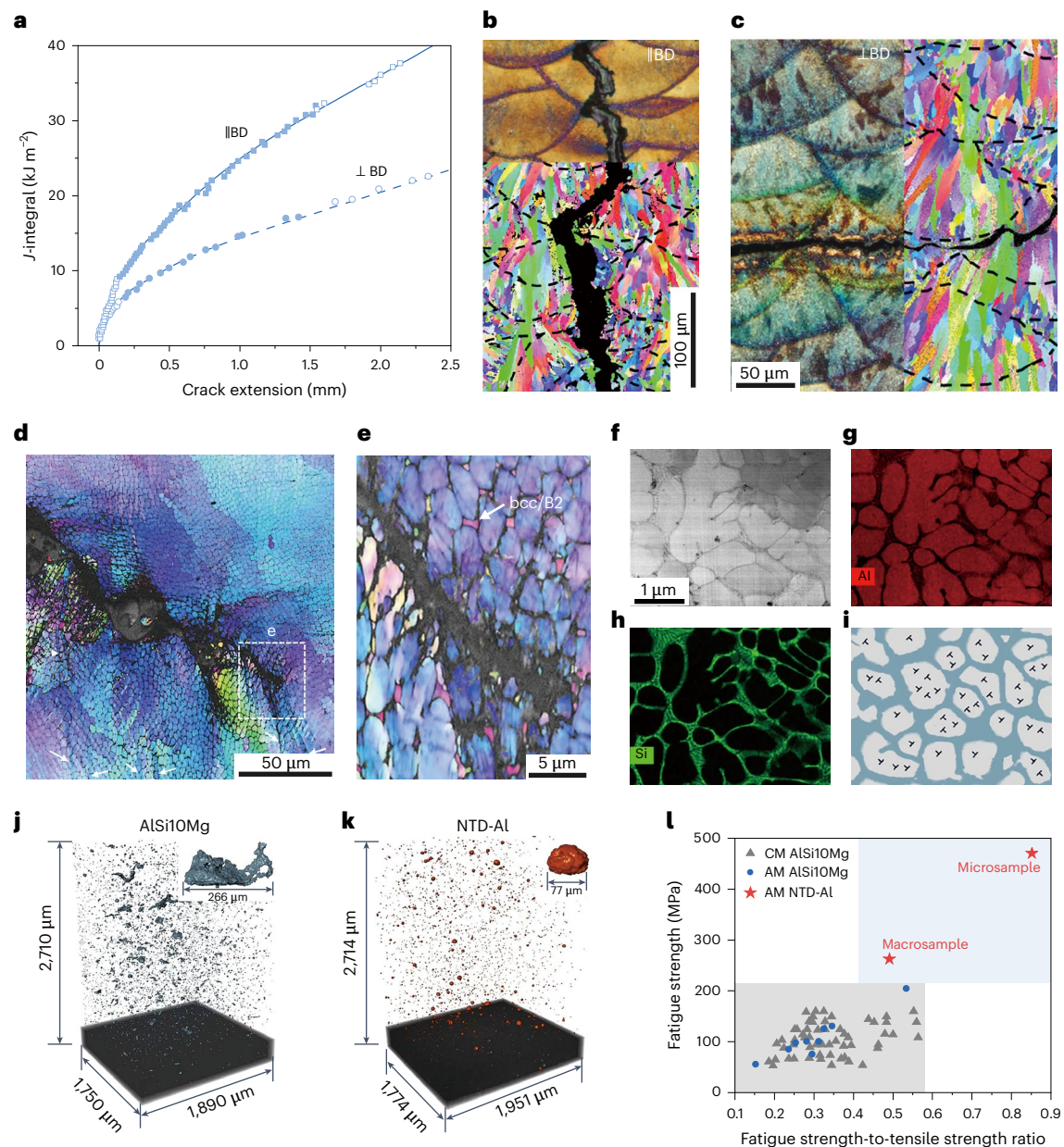


**Fig. 4 | Fracture and fatigue behaviour of AM metals.** **a**,  $J$ -integral-based crack resistance of L-PBF-produced AlSi10Mg alloys with the crack growing in two different orientations with respect to the build direction (BD) shown in **b** and **c**<sup>27,56</sup>. **b**, Optical microscope image (upper) and electron backscatter diffraction inverse pole figure map (lower) showing a crack propagation path parallel to ( $\parallel$ ) the BD, with frequent crack deflection. **c**, Optical microscope image (left) and electron backscatter diffraction inverse pole figure map (right) showing a crack propagation path perpendicular to ( $\perp$ ) the BD, with less crack deflection. **d**, Electron backscatter diffraction inverse pole figure map from the wake of the crack in an L-PBF-produced CoCrFeNiAl<sub>0.5</sub> HEA sample, showing crack deflection and bands of misorientation spreading away from the crack (indicated by the white arrows)<sup>12</sup>. **e**, Magnified inverse pole figure map near the crack tip of the L-PBF CoCrFeNiAl<sub>0.5</sub> HEA, showing misorientation bands traversing through the solidification cellular structures and crack deflection along the cell boundaries<sup>12</sup>. **f**, TEM image of solidification cellular structures

in L-PBF-produced NTD-Al alloy<sup>13</sup>. **g, h**, Elemental distribution maps of Al (**g**) and Si (**h**)<sup>13</sup>. **i**, Schematic of fatigue mechanisms in L-PBF NTD-Al, where the cellular structures act as volumetric dislocation cages to trap dislocations under cyclic loading for reducing localized fatigue damage<sup>13</sup>. **j**, Microcomputed tomography analysis showing printing defects with irregular morphology in the AM AlSi10Mg alloy<sup>13</sup>. The inset shows the maximum defect with a length of about 266  $\mu\text{m}$ . **k**, Microcomputed tomography analysis showing printing defects with near-spherical morphology in the AM NTD-Al alloy<sup>13</sup>. The inset shows the maximum defect with a diameter of about 77  $\mu\text{m}$ . **l**, Fatigue limit-to-tensile strength ratio versus fatigue strength of AM NTD-Al alloy, compared with CM and other AM AlSi10Mg alloys (stress ratio  $R = -1$ ). The specific alloys corresponding to the CM and AM AlSi10Mg datapoints can be found in ref. 13 and refs. 64–68, respectively. Panels adapted with permission from: **a–c**, ref. 56 under a Creative Commons license [CC BY 4.0](https://creativecommons.org/licenses/by/4.0/); **d, e**, ref. 12, Springer Nature Limited; **f–l**, ref. 13, Springer Nature Limited.

is commonly used in aerospace for its superior strength and resistance to creep and oxidation at elevated temperatures<sup>30</sup>. The favourable high-temperature properties of IN718 are mainly attributed to the precipitation-hardening effects of finely dispersed  $\gamma'$  ( $\text{Ni}_3\text{Nb}$ ) and  $\gamma''$  ( $\text{Ni}_3(\text{Ti,Al})$ ) nanoparticles.

AM IN718 superalloys show different creep properties compared with their CM counterparts due to distinct microstructures and phase constituents. The minimum creep rate versus applied stress was measured for both AM and CM IN718 alloys tested at 630 °C (Fig. 5a). The AM samples underwent three different heat-treatment protocols: 930 °C

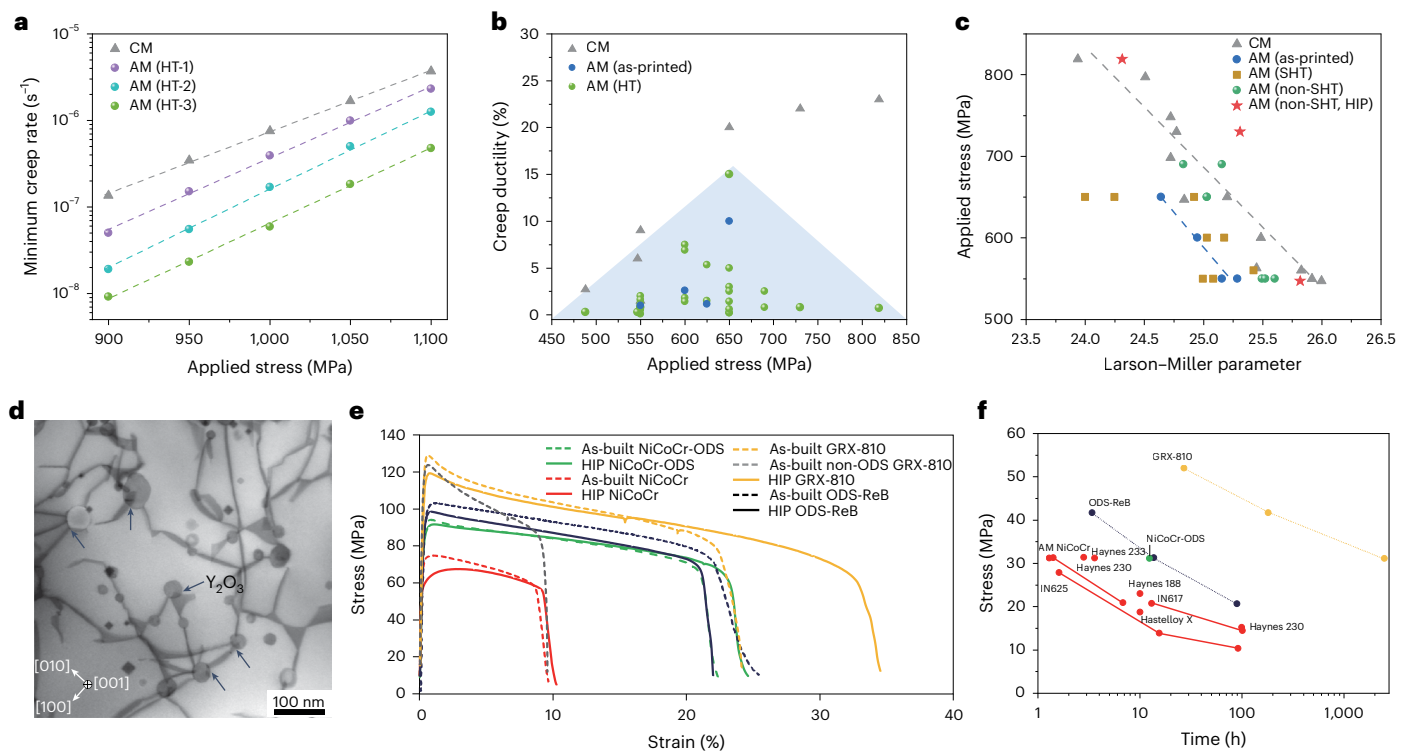


**Fig. 5 | Creep behaviour of AM metals.** **a**, Minimum creep rate versus applied stress for AM and CM IN718 superalloys tested at 630 °C. HT-1, HT-2 and HT-3 represent three different heat-treatment (HT) methods<sup>69</sup>. **b**, Creep ductility as a function of applied stress for AM and CM IN718 superalloys tested at 650 °C (refs. 71–81). The blue-shaded area represents AM samples in as-printed state or after HT. **c**, Comparison of the creep properties of AM and CM IN718 alloys<sup>71–81</sup> using the Larson–Miller parameter,  $LMP = (T + 273) \times (25 + \log_{10} t) / 1,000$ , where  $T$  is the temperature and  $t$  is the creep rupture lifetime. AM samples subjected to

SHT, non-SHT and hot isostatic pressing (HIP) are included in the comparison. **d**, TEM micrograph of GRX-810 ODS HEA, where the black arrows indicate  $Y_2O_3$  nanoparticles<sup>15</sup>. **e**, Tensile stress–strain behaviour of GRX-810 tested at 1,093 °C, compared with other HEA and ODS HEA variants<sup>15</sup>. ODS-ReB, NiCoCr-ODS with minor additions of Re (1.5 wt%) and B (0.03 wt%). **f**, Creep rupture lifetime of GRX-810 tested at 1,093 °C, compared with other Ni-based superalloys, NiCoCr HEA and ODS HEA variants<sup>15</sup>. Panels adapted with permission from: **a**, ref. 69, Elsevier; **d–f**, ref. 15, Springer Nature Limited.

solution plus ageing (HT-1), direct ageing (HT-2), and 1,000 °C solution plus ageing (HT-3)<sup>69</sup>. These samples demonstrate substantially lower creep rates, indicating a higher creep strength compared with conventional IN718 counterparts. This improved creep strength in AM IN718 arises mainly from a higher amount of  $\gamma''$  precipitates. Specifically, slow solidification in CM IN718 can cause macro-segregation of alloying elements such as Nb, resulting in undesired Laves and  $\delta$  intermetallic phases at interdendritic regions or grain boundaries, which deplete Nb in the matrix and hinder  $\gamma''$  precipitation during ageing<sup>70</sup>. By contrast, rapid solidification in AM IN718 creates a supersaturated  $\gamma$  matrix with reduced amounts of intermetallic Laves and  $\delta$  phases, whereas post-printing heat treatment promotes increased  $\gamma''$  precipitation from the supersaturated  $\gamma$  matrix<sup>69</sup>. Notably, the differences in creep strength between the AM samples with various heat-treatment protocols in Fig. 5a are also due to the varying amounts of intermetallic phases and  $\gamma''$  precipitates, highlighting the importance of heat treatment in optimizing the creep performance in AM superalloys. So far, most heat-treatment procedures for AM IN718 have been adopted from the industry standard heat treatment (SHT) developed for CM IN718 superalloy<sup>71–74</sup>.

Although AM IN718 superalloys have a higher creep strength, their resistance to creep rupture is generally lower than that of their CM counterparts. Creep rupture responses are compared in terms of creep ductility for AM and CM IN718 alloys tested at 650 °C (refs. 71–81; Fig. 5b). The AM samples consistently exhibit lower and more variable creep ductility compared with the CM counterparts. The embrittlement in AM IN718 alloys arises primarily from columnar grains with fine grain sizes and impurity—for example, sulfur—segregation at grain

boundaries, even after SHT<sup>81,82</sup>. The large grain boundary area provides more sites for cavity nucleation and growth, which are key mechanisms of creep failure in AM IN718<sup>72</sup> and other superalloys such as IN738LC<sup>83</sup>. The columnar grains also cause strong creep anisotropy, with the transverse direction being especially vulnerable to creep rupture<sup>71,82</sup>. Printing defects, such as lack-of-fusion pores and keyholes, can also accelerate cavitation, further reducing creep ductility and increasing variability in AM metals<sup>30</sup>.

Creep properties of AM and CM IN718 alloys<sup>71–81</sup> are compared using the Larson–Miller parameter (LMP), which relates the creep rupture time to temperature and stress, with higher LMP values indicating a better creep resistance (Fig. 5c). The comparison shows that AM IN718 samples, both as-printed and after SHT, underperform compared with their conventional counterparts due to lower creep ductility, even though they have a higher creep strength. However, the creep performance of AM IN718 can be improved with non-standard heat treatment (non-SHT). For example, high-temperature homogenization (1,080 °C for 12 h) dissolves the harmful Laves phase at grain boundaries and releases Nb into the matrix, promoting  $\gamma''$  precipitation during subsequent ageing<sup>79</sup>. This dissolution effect also reduces cavity nucleation sites. Moreover, homogenization recrystallizes columnar grains into larger equiaxed grains, reducing the number of grain boundaries prone to cavitation and cracking, thereby increasing the creep life and eliminating creep anisotropy. Hot isostatic pressing can also effectively remove printing defects, further enhancing the creep performance of AM IN718 (Fig. 5c). These findings indicate that the SHT protocols developed for CM metals may not be optimal for AM metals, which require customized heat treatments to enhance their mechanical properties.

The design of creep-resistant precipitation-hardened alloys is often constrained by the low volume fraction and rapid coarsening of precipitates at high temperatures<sup>84</sup>. Eutectic alloys with thermally stable intermetallic phases offer a solution to this issue. For example, a recently developed AM Al–Ce–Ni–Mn–Zr eutectic alloy<sup>16</sup> has demonstrated outstanding creep resistance up to 400 °C. Its microstructure features a continuous network of ~27% intermetallic phase (Al<sub>27</sub>Ni<sub>6</sub>Ce<sub>3</sub>), which is 10–100 times higher than the volume fraction of 0.3–3% that is typically found in precipitation-hardened Al alloys. Notably, the alloying elements in the Al–Ce–Ni–Mn–Zr alloy are selected for their low diffusivity in Al, making the intermetallic phase resistant to coarsening. The high content of the intermetallic phase, along with the fast cooling rates of additive manufacturing, refines the eutectic microstructure, achieving an ultrafine inter-phase spacing below 100 nm. This stable, finely distributed intermetallic phase effectively hinders dislocation motion, providing long-term creep resistance. As a result, the AM Al–Ce–Ni–Mn–Zr alloy shows creep rates at 400 °C that are orders of magnitude slower than those of other CM and AM creep-resistant Al alloys<sup>16</sup>.

The demand for advanced materials that can withstand extreme conditions, such as temperatures above 800 °C, is increasing in areas such as space exploration and energy production. High-temperature superalloys often struggle at these high temperatures owing to the rapid softening of their strengthening intermetallic phases and precipitates. By contrast, refractory alloys and ceramic-reinforced metal matrix composites show excellent strength and creep resistance under these conditions<sup>85–87</sup>. As refractory alloys are typically difficult to print because of cracking issues<sup>88</sup>, the additive manufacturing of metal matrix composites is more promising. A notable example is an oxide-dispersion-strengthened (ODS) HEA<sup>15</sup>. To develop this system, thermodynamic modelling was used to design a NiCoCr-based HEA with alloying elements including Al, Ti, Nb, Re, W and C. These elements were selected to improve both solid-solution strengthening and high-temperature stability while ensuring printability. Nanoscale Y<sub>2</sub>O<sub>3</sub> particles were coated onto the HEA powders and evenly distributed in the HEA matrix after L-PBF (Fig. 5d), resulting in an AM alloy called GRX-810. The superb tensile strength and ductility of GRX-810 at 1,093 °C are comparable to other NiCoCr and ODS variants (Fig. 5e). Its creep rupture lifetime is substantially longer, outperforming Ni-based superalloys such as IN617, IN625 and Haynes 230 at 1,093 °C (Fig. 5f). The outstanding performance of GRX-810 is attributed to the strengthening effects of oxide nanoparticles, stable MC carbides (where M is metal and C is carbon) and solute segregation of W, Cr and Re along grain boundaries, as guided by thermodynamic modelling. These heterogeneities protect the alloy from grain boundary failure, such as creep void formation and oxidation.

## Outlook

AM metals have unique hierarchical and heterogeneous microstructures, shaped by steep temperature gradients, rapid solidification and complex thermal cycling that are inherent to the line-by-line, layer-by-layer printing process. These non-equilibrium microstructures typically yield mechanical properties that are unattainable via conventional manufacturing. The mechanical behaviour of AM metals depends strongly on the alloy composition, processing parameters and post-processing treatments. Microstructural heterogeneity across multiple scales frequently produces anisotropic and variable mechanical properties, and printing-induced defects can further degrade strength, ductility and stability. Below, we outline key research needs and emerging opportunities to enhance the mechanical properties of AM metals through advances in processing control, alloy design, high-fidelity computational modelling and machine learning.

As a consequence of the large number of processing parameters involved in additive manufacturing, controlling the solidification microstructure and printing defects remains challenging. The use

of real-time characterization techniques, such as high-speed operando synchrotron X-ray imaging and diffraction, has enabled the in situ probing of laser–matter interactions and complex printing processes with high spatial and temporal resolution<sup>89</sup>. These techniques provide detailed information on melt pool flow, powder and liquid spatters, vapour depressions, thermal gradients, solidification rates, phase evolution and stress development during non-equilibrium transformations<sup>90–92</sup>. These results shed light on the formation and evolution of printing defects, offering guidance for process optimization to control microstructures and reduce defects<sup>93–95</sup>.

The shape and intensity of the laser beam strongly affect the melt pool geometry and temperature profiles during laser additive manufacturing. As a result, tailoring the laser beam profile has emerged as an effective method for controlling the melt pool dynamics and the resulting solidification microstructure. Approaches such as laser beam shaping<sup>96–98</sup>, pulsing<sup>99</sup>, oscillation<sup>100</sup> and polarization<sup>101</sup> have influenced key features such as grain size, shape and texture in AM metals. For example, changing a circular beam profile to an elliptical one can reshape the melt pool, enhance nucleation and promote fine equiaxed grains with reduced texture<sup>96,98</sup>. This strategy enables site-specific microstructure control for improving the mechanical performance. Furthermore, auxiliary ultrasound and magnetic fields show promise for additional control of solidification behaviour in AM metals<sup>102,103</sup>. Post-processing treatments, such as heat treatment and hot isostatic pressing, can further tailor microstructures and reduce defects. Given the unique microstructures, phases and compositional gradients in AM metals, customized heat-treatment and hot-isostatic-pressing protocols are needed to fully realize their potential.

Alloy design is another powerful approach for enhancing the mechanical performance of AM metals. Most commercial alloys were developed for conventional manufacturing and are not optimized for additive manufacturing. Rapid solidification during additive manufacturing can cause undesirable microstructures, such as coarse columnar grains and various cracking modes<sup>37</sup>. Therefore, designing material systems that are specific for additive manufacturing is essential. One strategy involves inoculation by adding nucleants to promote heterogeneous nucleation<sup>37</sup>. Alternatively, microalloying can induce strong constitutional supercooling at the solidification front, promoting grain refinement<sup>11,28</sup>. These metallurgical strategies facilitate a transition from columnar to fine equiaxed grains and reduce residual stresses, preventing cracking and improving the mechanical properties.

To support alloy design, computational modelling has been applied to characterize rapid solidification in additive manufacturing<sup>104</sup>. For instance, thermodynamic and kinetic models can determine freezing ranges to avoid solidification cracking, simulate precipitation and its thermomechanical impact to prevent strain-age cracking, and predict phase stability across temperature ranges<sup>105</sup>. Other models, including heat transfer, fluid dynamics, phase field, Monte Carlo and cellular automata, can help to understand solidification phases and microstructural morphology, leading to improved printability and material properties<sup>106</sup>. However, progress is limited by data scarcity, especially in complex multi-component systems. Emerging combinatorial additive-manufacturing methods enable the high-throughput synthesis of alloy libraries, facilitating the rapid discovery of novel AM-compatible alloys<sup>107</sup>. In addition, the unique nature of additive manufacturing enables the rethinking of alloy design through compositional simplification. This approach makes possible the printing of alloys with reduced complexity while achieving tailored microstructures and enhanced mechanical properties, as demonstrated in AM plain carbon steels<sup>108</sup> and Ti–O alloys<sup>109</sup>. The strategy of reducing compositional complexity aligns with sustainability goals, positioning additive manufacturing as a promising solution for eco-friendly materials innovation.

Additive manufacturing offers exceptional capability for site-specific tailoring of the microstructure by adjusting the process

parameters or feedstock composition during printing<sup>110</sup>. This enables the fabrication of functionally or structurally graded materials, where different parts of the same printed object can have varying compositions and/or microstructures<sup>111</sup>. In addition, mixing powders of different compositions enables deliberate chemical heterogeneity at meso- and micro-scales, improving control over phase distribution and deformation mechanisms<sup>112,113</sup>. In this context, mechanical strengthening from microstresses, especially back stresses, can be enhanced by heterogeneity tailoring. The resulting gradient plasticity and GNDs accommodate strain mismatches among various heterogeneous components, promoting sustained strain-hardening behaviour<sup>20</sup>. The engineered complexities in chemical composition and microstructure broaden the material design space, leading to improved mechanical properties in AM metals.

The non-equilibrium microstructures formed in AM metals often result in excellent mechanical properties and offer opportunities to further enhance their performance through post-processing<sup>9</sup>. However, these microstructures also raise concerns about thermal stability, as printing-induced features can transform or decompose at elevated temperatures. For example, in AM 316L stainless steel, studies have shown that the microstructure remains stable up to -600 °C, maintaining its strength, ductility and creep resistance due to stable cellular structures formed during solidification<sup>114–116</sup>. Between 600 °C and 1,000 °C, diffusion processes gradually dissolve these structures, leading to a decline in mechanical performance. Above 1,100 °C, full recrystallization occurs, and the unique AM microstructure is lost, making it similar to CM materials. These observations indicate that whereas AM metals can retain unique properties within certain temperature ranges, their performance may degrade at higher temperatures. Therefore, future research will need to focus on stabilizing these metastable microstructures for high-temperature applications.

Studying the mechanical properties of AM metals is time-consuming due to the vast processing parameter space and their complex microstructures. Computational models are increasingly used to bridge the processing, microstructure and mechanical behaviour of AM metals<sup>117,118</sup>. However, many traditional models overlook the unique features of additive manufacturing, such as cellular structures and printing defects, leading to limited predictive accuracy. High-fidelity models that incorporate AM-specific characteristics are therefore essential for reliable performance predictions. Advanced experimental techniques<sup>51</sup>, such as in situ microcomputed tomography, high-resolution digital image correlation and 3D X-ray diffraction microscopy, can further enhance these models with real microstructural data. In addition, machine learning is emerging as a powerful complement to mechanistic models in additive manufacturing, helping to overcome the limitations of traditional experimental trial-and-error approaches and data-scarce computational methods<sup>106</sup>. It provides a scalable means for exploring high-dimensional parameter spaces and uncovering processing–structure–property–performance relationships, thereby reducing the number of costly experiments<sup>119</sup>. Emerging models, such as physics-informed and generative machine learning, further open opportunities for intelligent automation across the additive-manufacturing workflow<sup>120</sup>. With rapid progress in processing control, alloy design, advanced characterization, computational modelling and machine learning, additive manufacturing is poised to revolutionize the development of next-generation structural materials with superior mechanical properties.

## References

1. DebRoy, T. et al. Scientific, technological and economic issues in metal printing and their solutions. *Nat. Mater.* **18**, 1026–1032 (2019).
2. Gu, D. et al. Material-structure-performance integrated laser-metal additive manufacturing. *Science* **372**, eabg1487 (2021).
3. Blakey-Milner, B. et al. Metal additive manufacturing in aerospace: a review. *Mater. Des.* **209**, 110008 (2021).
4. Pham, M.-S., Liu, C., Todd, I. & Lertthanasarn, J. Damage-tolerant architected materials inspired by crystal microstructure. *Nature* **565**, 305–311 (2019).
5. DebRoy, T. et al. Additive manufacturing of metallic components—process, structure and properties. *Prog. Mater. Sci.* **92**, 112–224 (2018).
6. Mukherjee, T. et al. Control of grain structure, phases, and defects in additive manufacturing of high-performance metallic components. *Prog. Mater. Sci.* **138**, 101153 (2023).
7. Collins, P. C., Brice, D. A., Samimi, P., Ghamarian, I. & Fraser, H. L. Microstructural control of additively manufactured metallic materials. *Annu. Rev. Mater. Res.* **46**, 63–91 (2016).
8. Wang, Y. M. et al. Additively manufactured hierarchical stainless steels with high strength and ductility. *Nat. Mater.* **17**, 63–71 (2018).
9. Ren, J. et al. Strong yet ductile nanolamellar high-entropy alloys by additive manufacturing. *Nature* **608**, 62–68 (2022).
10. Song, T. et al. Strong and ductile titanium–oxygen–iron alloys by additive manufacturing. *Nature* **618**, 63–68 (2023).
11. Zhang, J. et al. Ultrauniform, strong, and ductile 3D-printed titanium alloy through bifunctional alloy design. *Science* **383**, 639–645 (2024).
12. Kumar, P. et al. A strong fracture-resistant high-entropy alloy with nano-bridged honeycomb microstructure intrinsically toughened by 3D-printing. *Nat. Commun.* **15**, 841 (2024).
13. Dan, C. et al. Achieving ultrahigh fatigue resistance in AlSi10Mg alloy by additive manufacturing. *Nat. Mater.* **22**, 1182–1188 (2023).
14. Qu, Z. et al. High fatigue resistance in a titanium alloy via near-void-free 3D printing. *Nature* **626**, 999–1004 (2024).
15. Smith, T. M. et al. A 3D printable alloy designed for extreme environments. *Nature* **617**, 513–518 (2023).
16. Bahl, S. et al. An additively manufactured near-eutectic Al-Ce-Ni-Mn-Zr alloy with high creep resistance. *Acta Mater.* **268**, 119787 (2024).
17. Herzog, D., Seyda, V., Wycisk, E. & Emmelmann, C. Additive manufacturing of metals. *Acta Mater.* **117**, 371–392 (2016).
18. Lewandowski, J. J. & Seifi, M. Metal additive manufacturing: a review of mechanical properties. *Annu. Rev. Mater. Res.* **46**, 151–186 (2016).
19. Hart, E. Theory of the tensile test. *Acta Metall.* **15**, 351–355 (1967).
20. Ma, E. & Zhu, T. Towards strength–ductility synergy through the design of heterogeneous nanostructures in metals. *Mater. Today* **20**, 323–331 (2017).
21. Zhu, Y. et al. Heterostructured materials: superior properties from hetero-zone interaction. *Mater. Res. Lett.* **9**, 1–31 (2021).
22. Tao, N. R. et al. An investigation of surface nanocrystallization mechanism in Fe induced by surface mechanical attrition treatment. *Acta Mater.* **50**, 4603–4616 (2002).
23. Prashanth, K. G. & Eckert, J. Formation of metastable cellular microstructures in selective laser melted alloys. *J. Alloys Compd.* **707**, 27–34 (2017).
24. Pham, M.-S., Dovggy, B., Hooper, P. A., Gourlay, C. M. & Piglione, A. The role of side-branching in microstructure development in laser powder-bed fusion. *Nat. Commun.* **11**, 749 (2020).
25. Bajaj, P. et al. Steels in additive manufacturing: a review of their microstructure and properties. *Mater. Sci. Eng. A* **772**, 138633 (2020).
26. Kürnsteiner, P. et al. High-strength Damascus steel by additive manufacturing. *Nature* **582**, 515–519 (2020).
27. Paul, M. J. et al. Fracture resistance of AlSi10Mg fabricated by laser powder bed fusion. *Acta Mater.* **211**, 116869 (2021).
28. Zhang, D. et al. Additive manufacturing of ultrafine-grained high-strength titanium alloys. *Nature* **576**, 91–95 (2019).

29. Zhu, Y. et al. Ultrastrong nanotwinned titanium alloys through additive manufacturing. *Nat. Mater.* **21**, 1258–1262 (2022).
30. Mostafaei, A. et al. Additive manufacturing of nickel-based superalloys: a state-of-the-art review on process-structure-defect-property relationship. *Prog. Mater. Sci.* **136**, 101108 (2023).
31. Zhu, Z. G. et al. Hierarchical microstructure and strengthening mechanisms of a CoCrFeNiMn high entropy alloy additively manufactured by selective laser melting. *Scr. Mater.* **154**, 20–24 (2018).
32. Shao, J. et al. Grain size evolution under different cooling rate in laser additive manufacturing of superalloy. *Opt. Laser Technol.* **119**, 105662 (2019).
33. Liu, P. et al. Insight into the mechanisms of columnar to equiaxed grain transition during metallic additive manufacturing. *Addit. Manuf.* **26**, 22–29 (2019).
34. Xu, J. et al. Grain refinement and crack inhibition of hard-to-weld Inconel 738 alloy by altering the scanning strategy during selective laser melting. *Mater. Des.* **209**, 109940 (2021).
35. Zhang, G. et al. In-situ grain structure control in directed energy deposition of Ti6Al4V. *Addit. Manuf.* **55**, 102865 (2022).
36. Li, X. P. et al. Selective laser melting of nano-TiB<sub>2</sub> decorated AlSi10Mg alloy with high fracture strength and ductility. *Acta Mater.* **129**, 183–193 (2017).
37. Martin, J. H. et al. 3D printing of high-strength aluminium alloys. *Nature* **549**, 365–369 (2017).
38. Bermingham, M. J., StJohn, D. H., Krynen, J., Tedman-Jones, S. & Dargusch, M. S. Promoting the columnar to equiaxed transition and grain refinement of titanium alloys during additive manufacturing. *Acta Mater.* **168**, 261–274 (2019).
39. Qu, S. et al. Oxide-dispersion-enabled laser additive manufacturing of high-resolution copper. *Nat. Commun.* **16**, 3234 (2025).
40. Han, Q. et al. Additive manufacturing of high-strength crack-free Ni-based Hastelloy X superalloy. *Addit. Manuf.* **30**, 100919 (2019).
41. Wang, Y. L., Zhao, L., Wan, D., Guan, S. & Chan, K. C. Additive manufacturing of TiB<sub>2</sub>-containing CoCrFeMnNi high-entropy alloy matrix composites with high density and enhanced mechanical properties. *Mater. Sci. Eng. A* **825**, 141871 (2021).
42. Dye, D., Stone, H. J. & Reed, R. C. Intergranular and interphase microstresses. *Curr. Opin. Solid State Mater. Sci.* **5**, 31–37 (2001).
43. Cheng, Z., Zhou, H., Lu, Q., Gao, H. & Lu, L. Extra strengthening and work hardening in gradient nanotwinned metals. *Science* **362**, eaau1925 (2018).
44. Pan, Q. et al. Gradient cell-structured high-entropy alloy with exceptional strength and ductility. *Science* **374**, 984–989 (2021).
45. Cheng, Z. et al. Unraveling the origin of extra strengthening in gradient nanotwinned metals. *Proc. Natl Acad. Sci. USA* **119**, e2116808119 (2022).
46. Zhang, Y., Cheng, Z., Zhu, T. & Lu, L. Mechanics of gradient nanostructured metals. *J. Mech. Phys. Solids* **189**, 105719 (2024).
47. Chen, W. et al. Microscale residual stresses in additively manufactured stainless steel. *Nat. Commun.* **10**, 4338 (2019).
48. Jia, D., Ramesh, K. T. & Ma, E. Effects of nanocrystalline and ultrafine grain sizes on constitutive behavior and shear bands in iron. *Acta Mater.* **51**, 3495–3509 (2003).
49. Schuren, J. C. et al. New opportunities for quantitative tracking of polycrystal responses in three dimensions. *Curr. Opin. Solid State Mater. Sci.* **19**, 235–244 (2015).
50. Sangid, M. D. et al. Role of heat treatment and build orientation in the microstructure sensitive deformation characteristics of IN718 produced via SLM additive manufacturing. *Addit. Manuf.* **22**, 479–496 (2018).
51. Stinville, J. C. et al. Insights into plastic localization by crystallographic slip from emerging experimental and numerical approaches. *Annu. Rev. Mater. Res.* **53**, 275–317 (2023).
52. Zhang, Y. et al. Modeling of microscale internal stresses in additively manufactured stainless steel. *Model. Simul. Mater. Sci. Eng.* **30**, 074001 (2022).
53. Jeong, S. G. et al. Architected heterogeneous alloys with selective laser melting. *Scr. Mater.* **208**, 114332 (2022).
54. Gao, S. et al. Additive manufacturing of alloys with programmable microstructure and properties. *Nat. Commun.* **14**, 6752 (2023).
55. Becker, T. H., Kumar, P. & Ramamurty, U. Fracture and fatigue in additively manufactured metals. *Acta Mater.* **219**, 117240 (2021).
56. Paul, M. J., Kruzic, J. J., Ramamurty, U. & Gludovatz, B. The importance of fracture toughness evaluation for additively manufactured metals. *Acta Mater.* **276**, 120061 (2024).
57. de Menezes, J. T. O., Castrodeza, E. M. & Casati, R. Effect of build orientation on fracture and tensile behavior of A357 Al alloy processed by selective laser melting. *Mater. Sci. Eng. A* **766**, 138392 (2019).
58. Mostafaei, A. et al. Defects and anomalies in powder bed fusion metal additive manufacturing. *Curr. Opin. Solid State Mater. Sci.* **26**, 100974 (2022).
59. Cain, V., Thijs, L., Van Humbeeck, J., Van Hooreweder, B. & Knutsen, R. Crack propagation and fracture toughness of Ti6Al4V alloy produced by selective laser melting. *Addit. Manuf.* **5**, 68–76 (2015).
60. Kumar, P., Prakash, O. & Ramamurty, U. Micro- and meso-structures and their influence on mechanical properties of selectively laser melted Ti-6Al-4V. *Acta Mater.* **154**, 246–260 (2018).
61. Liu, H. et al. Review on fatigue of additive manufactured metallic alloys: microstructure, performance, enhancement, and assessment methods. *Adv. Mater.* **36**, 2306570 (2024).
62. Murakami, Y., Takagi, T., Wada, K. & Matsunaga, H. Essential structure of S-N curve: prediction of fatigue life and fatigue limit of defective materials and nature of scatter. *Int. J. Fatigue* **146**, 106138 (2021).
63. Qu, M. et al. Controlling process instability for defect lean metal additive manufacturing. *Nat. Commun.* **13**, 1079 (2022).
64. Mower, T. M. & Long, M. J. Mechanical behavior of additive manufactured, powder-bed laser-fused materials. *Mater. Sci. Eng. A* **651**, 198–213 (2016).
65. Awd, M. et al. Comparison of microstructure and mechanical properties of Scalmetal<sup>®</sup> produced by selective laser melting and laser metal deposition. *Materials* **11**, 17 (2017).
66. Uzan, N. E., Shneck, R., Yeheskel, O. & Frage, N. Fatigue of AlSi10Mg specimens fabricated by additive manufacturing selective laser melting (AM-SLM). *Mater. Sci. Eng. A* **704**, 229–237 (2017).
67. Ngnekou, J. N. D. et al. Fatigue properties of AlSi10Mg produced by additive layer manufacturing. *Int. J. Fatigue* **119**, 160–172 (2019).
68. Sausto, F., Carrion, P. E., Shamsaei, N. & Beretta, S. Fatigue failure mechanisms for AlSi10Mg manufactured by L-PBF under axial and torsional loads: the role of defects and residual stresses. *Int. J. Fatigue* **162**, 106903 (2022).
69. Pröbstle, M. et al. Superior creep strength of a nickel-based superalloy produced by selective laser melting. *Mater. Sci. Eng. A* **674**, 299–307 (2016).
70. Manikandan, S. G. K., Sivakumar, D., Prasad Rao, K. & Kamaraj, M. Laves phase in alloy 718 fusion zone—microscopic and calorimetric studies. *Mater. Charact.* **100**, 192–206 (2015).
71. Kuo, Y.-L., Horikawa, S. & Kakehi, K. Effects of build direction and heat treatment on creep properties of Ni-base superalloy built up by additive manufacturing. *Scr. Mater.* **129**, 74–78 (2017).

72. Xu, Z., Murray, J. W., Hyde, C. J. & Clare, A. T. Effect of post processing on the creep performance of laser powder bed fused Inconel 718. *Addit. Manuf.* **24**, 486–497 (2018).
73. Shi, J. J. et al. Study on the microstructure and creep behavior of Inconel 718 superalloy fabricated by selective laser melting. *Mater. Sci. Eng. A* **765**, 138282 (2019).
74. Xu, Z. et al. Creep property of Inconel 718 superalloy produced by selective laser melting compared to forging. *Mater. Sci. Eng. A* **794**, 139947 (2020).
75. Kim, D.-H. et al. Stress rupture characteristics of Inconel 718 alloy for ramjet combustor. *Mater. Sci. Eng. A* **483–484**, 262–265 (2008).
76. Kuo, C.-M., Yang, Y.-T., Bor, H.-Y., Wei, C.-N. & Tai, C.-C. Aging effects on the microstructure and creep behavior of Inconel 718 superalloy. *Mater. Sci. Eng. A* **510–511**, 289–294 (2009).
77. Kuo, Y.-L., Nagahari, T. & Kakehi, K. The effect of post-processes on the microstructure and creep properties of Alloy718 built up by selective laser melting. *Materials* **11**, 996 (2018).
78. Sanchez, S. et al. The creep behaviour of nickel alloy 718 manufactured by laser powder bed fusion. *Mater. Des.* **204**, 109647 (2021).
79. Wu, S. et al. Improving creep property of additively manufactured Inconel 718 through specifically-designed post heat treatments. *Mater. Sci. Eng. A* **857**, 144047 (2022).
80. Wang, L. et al. Improved creep properties of Inconel 718 fabricated by selective laser melting from boron–phosphorus interaction. *Mater. Res. Lett.* **12**, 661–667 (2024).
81. Oros, T. J., Son, K., Hodge, A. M. & Kassner, M. E. The high temperature creep and fracture behavior of Inconel 718 produced by additive manufacturing. *Scr. Mater.* **251**, 116208 (2024).
82. Shi, J. J. et al. Microstructure and creep anisotropy of Inconel 718 alloy processed by selective laser melting. *Mater. Sci. Eng. A* **805**, 140583 (2021).
83. Xu, J., Gruber, H., Deng, D., Peng, R. L. & Moverare, J. J. Short-term creep behavior of an additive manufactured non-weldable nickel-base superalloy evaluated by slow strain rate testing. *Acta Mater.* **179**, 142–157 (2019).
84. Boyd, J. D. & Nicholson, R. B. The coarsening behaviour of  $\theta''$  and  $\theta'$  precipitates in two Al–Cu alloys. *Acta Metall.* **19**, 1379–1391 (1971).
85. Yamabe-Mitarai, Y., Ro, Y., Harada, H. & Maruko, T. Ir-base refractory superalloys for ultra-high temperatures. *Metall. Mater. Trans. A* **29**, 537–549 (1998).
86. Kamata, S. Y. et al. Ultrahigh-temperature tensile creep of TiC-reinforced Mo–Si–B-based alloy. *Sci. Rep.* **8**, 10487 (2018).
87. Tekoglu, E. et al. Superior high-temperature mechanical properties and microstructural features of LPBF-printed In625-based metal matrix composites. *Mater. Today* **80**, 297–307 (2024).
88. Talignani, A. et al. A review on additive manufacturing of refractory tungsten and tungsten alloys. *Addit. Manuf.* **58**, 103009 (2022).
89. Zhao, C. et al. Real-time monitoring of laser powder bed fusion process using high-speed X-ray imaging and diffraction. *Sci. Rep.* **7**, 3602 (2017).
90. Cunningham, R. et al. Keyhole threshold and morphology in laser melting revealed by ultrahigh-speed X-ray imaging. *Science* **363**, 849–852 (2019).
91. Chen, Y. et al. Correlative synchrotron X-ray imaging and diffraction of directed energy deposition additive manufacturing. *Acta Mater.* **209**, 116777 (2021).
92. Chen, Y. et al. In situ observation and reduction of hot-cracks in laser additive manufacturing. *Commun. Mater.* **5**, 84 (2024).
93. Leung, C. L. A. et al. In situ X-ray imaging of defect and molten pool dynamics in laser additive manufacturing. *Nat. Commun.* **9**, 1355 (2018).
94. Hojjatzadeh, S. M. H. et al. Pore elimination mechanisms during 3D printing of metals. *Nat. Commun.* **10**, 3088 (2019).
95. Martin, A. A. et al. Dynamics of pore formation during laser powder bed fusion additive manufacturing. *Nat. Commun.* **10**, 1987 (2019).
96. Roehling, T. T. et al. Modulating laser intensity profile ellipticity for microstructural control during metal additive manufacturing. *Acta Mater.* **128**, 197–206 (2017).
97. Roehling, T. T. et al. Controlling grain nucleation and morphology by laser beam shaping in metal additive manufacturing. *Mater. Des.* **195**, 109071 (2020).
98. Shi, R. et al. Microstructural control in metal laser powder bed fusion additive manufacturing using laser beam shaping strategy. *Acta Mater.* **184**, 284–305 (2020).
99. Gao, S. et al. Pulsed-wave laser additive manufacturing of CrCoNi medium-entropy alloys with high strength and ductility. *Mater. Today* **81**, 36–46 (2024).
100. Dai, G. et al. Grain refinement and columnar-to-equiaxed transition of Ti6Al4V during additive manufacturing via different laser oscillations. *Int. J. Mach. Tools Manuf.* **189**, 104031 (2023).
101. Grünewald, J., Blickle, V., Allenberg-Rabe, M., Wagenblast, P. & Wudy, K. Flexible and highly dynamic beam shaping for laser-based powder bed fusion of metals. *Procedia CIRP* **111**, 65–70 (2022).
102. Todaro, C. J. et al. Grain structure control during metal 3D printing by high-intensity ultrasound. *Nat. Commun.* **11**, 142 (2020).
103. Tan, C. et al. Review on field assisted metal additive manufacturing. *Int. J. Mach. Tools Manuf.* **189**, 104032 (2023).
104. Pollock, T. M., Clarke, A. J. & Babu, S. S. Design and tailoring of alloys for additive manufacturing. *Metall. Mater. Trans. A* **51**, 6000–6019 (2020).
105. Tang, Y. T. et al. Alloys-by-design: application to new superalloys for additive manufacturing. *Acta Mater.* **202**, 417–436 (2021).
106. DebRoy, T., Mukherjee, T., Wei, H. L., Elmer, J. W. & Milewski, J. O. Metallurgy, mechanistic models and machine learning in metal printing. *Nat. Rev. Mater.* **6**, 48–68 (2021).
107. Moorehead, M. et al. High-throughput synthesis of Mo–Nb–Ta–W high-entropy alloys via additive manufacturing. *Mater. Des.* **187**, 108358 (2020).
108. Tan, Q. et al. High performance plain carbon steels obtained through 3D-printing. *Nat. Commun.* **15**, 10077 (2024).
109. Ding, W. et al. Lean design of a strong and ductile dual-phase titanium–oxygen alloy. *Nat. Mater.* **24**, 506–512 (2025).
110. Tammis-Williams, S. & Todd, I. Design for additive manufacturing with site-specific properties in metals and alloys. *Scr. Mater.* **135**, 105–110 (2017).
111. Reichardt, A. et al. Advances in additive manufacturing of metal-based functionally graded materials. *Int. Mater. Rev.* **66**, 1–29 (2021).
112. Zhang, T. et al. In situ design of advanced titanium alloy with concentration modulations by additive manufacturing. *Science* **374**, 478–482 (2021).
113. Li, H., Thomas, S. & Hutchinson, C. Delivering microstructural complexity to additively manufactured metals through controlled mesoscale chemical heterogeneity. *Acta Mater.* **226**, 117637 (2022).
114. Voisin, T. et al. New insights on cellular structures strengthening mechanisms and thermal stability of an austenitic stainless steel fabricated by laser powder-bed-fusion. *Acta Mater.* **203**, 116476 (2021).

115. Li, Y., Krajčák, T., Podaný, P., Veselý, J. & Džugan, J. Thermal stability of dislocation structure and its effect on creep property in austenitic 316L stainless steel manufactured by directed energy deposition. *Mater. Sci. Eng. A* **873**, 144981 (2023).
116. Pan, Y. et al. Creep behavior and fracture mechanism of an additively manufactured 316L stainless steel with extraordinary creep resistance. *Mech. Mater.* **196**, 105053 (2024).
117. Smith, J. et al. Linking process, structure, property, and performance for metal-based additive manufacturing: computational approaches with experimental support. *Comput. Mech.* **57**, 583–610 (2016).
118. Wu, S. et al. A microstructure-based creep model for additively manufactured nickel-based superalloys. *Acta Mater.* **224**, 117528 (2022).
119. Ng, W. L., Goh, G. L., Goh, G. D., Ten, J. S. J. & Yeong, W. Y. Progress and opportunities for machine learning in materials and processes of additive manufacturing. *Adv. Mater.* **36**, 2310006 (2024).
120. Jin, Z., Zhang, Z., Demir, K. & Gu, G. X. Machine learning for advanced additive manufacturing. *Matter* **3**, 1541–1556 (2020).

## Acknowledgements

T.Z. acknowledges support by the National Science Foundation (DMR-2004412) and the Office of Naval Research (N00014-18-1-2784). W.C. acknowledges support by the National Science Foundation (DMR-2004429 and DMR-2516550) and the Department of Energy-National Nuclear Security Administration Center of Excellence CAMCSE under award number DE-NA0004154. We thank J. Liu for assistance with data analysis.

## Author Contributions

T.Z. and W.C. contributed to the conceptualization, methodology, drafting and revision of the paper.

## Competing interests

The authors declare no competing interests.

## Additional information

**Correspondence and requests for materials** should be addressed to Ting Zhu or Wen Chen.

**Peer review information** *Nature Materials* thanks Xiaozhou Liao, Iain Todd and the other, anonymous, reviewer(s) for their contribution to the peer review of this work.

**Reprints and permissions information** is available at [www.nature.com/reprints](http://www.nature.com/reprints).

**Publisher's note** Springer Nature remains neutral with regard to jurisdictional claims in published maps and institutional affiliations.

Springer Nature or its licensor (e.g. a society or other partner) holds exclusive rights to this article under a publishing agreement with the author(s) or other rightsholder(s); author self-archiving of the accepted manuscript version of this article is solely governed by the terms of such publishing agreement and applicable law.

© Springer Nature Limited 2026